

Searching for and characterizing halo substructures with the GALAH DR4 survey

Iryna Kushniruk¹, Kristopher Youakim¹, Karin Lind¹, Sven Buder^{2,6}, Janes Kos⁴, Diane Feuillet⁸, Sarah L. Martell^{6,7}, Richard de Grijs^{5,9,10}, Geraint F. Lewis³, Joss Bland-Hawthorn^{3,6}, Gary Da Costa², Michael Hayden^{3,6}, Daniel Zucker^{5,6}, Tomaz Zwitter⁴, and Sanjib Sharma¹¹

¹ Department of Astronomy, Stockholm University, AlbaNova University Center, SE-106 91 Stockholm - Sweden

² Research School of Astronomy and Astrophysics, The Australian National University, Canberra ACT2611, Australia

³ Sydney Institute for Astronomy, School of Physics, A28, The University of Sydney, NSW 2006, Australia

⁴ Faculty of Mathematics and Physics, University of Ljubljana, Jadranska 19, 1000 Ljubljana, Slovenia

⁵ School of Mathematical and Physical Sciences, Macquarie University, Balaclava Road, Sydney, NSW 2109, Australia

⁶ ARC Centre of Excellence for All Sky Astrophysics in 3 Dimensions (ASTRO 3D), Australia

⁷ School of Physics, University of New South Wales, Sydney NSW 2052, Australia

⁸ Lund Observatory, Department of Geology, Sölvegatan 12, SE-223 62 Lund, Sweden

⁹ Astrophysics and Space Technologies Research Centre, Macquarie University, Balaclava Road, Sydney, NSW 2109, Australia

¹⁰ International Space Science Institute–Beijing, 1 Nanertiao, Zhongguancun, Hai Dian District, Beijing 100190, China

¹¹ Space Telescope Science Institute, 3700 San Martin Drive, Baltimore, MD 21218, USA

e-mail: iryna.kushniruk@astro.su.se

Received 20 June 2024 / Accepted 09 Feb 2026

ABSTRACT

Context. Recent studies have revealed that the Milky Way’s stellar halo is a composite of stellar populations of different origins, including multiple accretion events. To better understand how the Milky Way and other spiral galaxies were formed, it is necessary to thoroughly characterize the chemical and kinematic properties of these structures.

Aims. We search for kinematic structures of the stellar halo, find any substructures within them if present, and characterize the chemo-dynamical properties of the identified groups with the GALAH DR4 and *Gaia* surveys.

Methods. We apply wavelet transforms in the space defined by a square root of radial action (J_r) and azimuthal action (L_z) to search for kinematic overdensities. Then, we select stars in the detected structures and investigate their elemental abundances to determine their origin. Additionally, we check for any contamination from other stellar populations within the detected groups with the unsupervised machine learning algorithm t-Distributed Stochastic Neighbor Embedding (t-SNE), for which we perform chemical tagging in a high-dimensional parameter space using 15 elemental abundances as input.

Results. We recovered five kinematic structures in the action space with the wavelet transform. These groups are the Galactic disk, Splash, *Gaia*-Sausage-Enceladus (GSE), Thamnos1 and Thamnos2. We found that GSE has two peaks with the wavelet transform; one of these peaks is located at $\sqrt{J_r} \approx 25$ kpc km s⁻¹ and is a result of contamination from disk stars. The other peak corresponds to the ‘cleanest’ GSE population and is located above $\sqrt{J_r} \approx 40$ kpc km s⁻¹. We also detected three peaks in Thamnos. We linked two of them to Thamnos1 and the peak with the stars on the most retrograde orbits to Thamnos2. The t-SNE algorithm also confirmed these findings. We also analyzed individual elemental abundances of each group and found that Thamnos2 has a higher $[\alpha/\text{Fe}]$ ratio than the other groups, iron-peak elements are more abundant in the Splash than in the halo groups, while the halo structures retain a higher r-process signature than the splashed disk.

Conclusions. A multiply-peaked substructure we observe in action space in GSE and Thamnos suggests that the splashed disk extends beyond the borders of prograde orbits. Each of the four halo groups studied in this paper have unique chemo-dynamical properties that confirm their extra-galactic origin.

Key words. galaxy:kinematics and dynamics – galaxy:halo – galaxy:structure

1. Introduction

The formation and evolution process of large spiral galaxies is an active research area in modern astronomy. Since the Milky Way is the only galaxy whose stars and structures can be studied in great detail, it is a benchmark for constraining models of galaxy formation. Therefore, studying the formation of the Milky Way in great detail is crucial to our understanding of spiral galaxies in general.

It is known that the Galaxy contains many kinematic structures, and the nature and origins of these remain unresolved.

A vast number of currently known structures have been found in the Galactic halo and likely formed due to accretion events where small galaxies merged with the Milky Way (e.g. Helmi et al. 2018; Belokurov et al. 2018; Koppelman et al. 2019; Myeong et al. 2019; Helmi 2020; Naidu et al. 2020; Ji et al. 2020; Deason & Belokurov 2024). Since accreted stars retain similar chemical composition and motion to their progenitor (e.g. Freeman & Bland-Hawthorn 2002; Tolstoy et al. 2009), examining the chemo-dynamical properties of stars helps to separate accreted populations from those formed *in situ*. Thus, we need to have high-precision spectroscopic parameters and astro-

metric measurements for as many stars in the Galaxy as possible to discover new halo populations and characterize the already known ones.

Nowadays, large spectroscopic and astrometric surveys that provide data for millions of stars, and many millions more are expected in the near future. Current and future surveys include the Galactic Archaeology with HERMES (GALAH; [De Silva et al. 2015](#)), the Apache Point Observatory Galactic Evolution Experiment (APOGEE; [Holtzman et al. 2018](#)), the Large sky Area Multi-Object fibre Spectroscopic Telescope (LAMOST; [Zhao et al. 2012](#)), the Hectochelle in the Halo at High resolution survey (H3; [Conroy et al. 2019](#)), *Gaia* ([Lindegren et al. 2016](#)) and upcoming surveys like the 4-metre Multi-Object Spectroscopic Telescope (4MOST; [de Jong et al. 2019](#)) and the WHT Enhanced Area Velocity Explorer (WEAVE; [Dalton et al. 2018, 2020](#)) are expected to provide data on many more millions of stars. These and many other surveys provide the necessary data to explore halo debris, which has led to several discoveries. For instance, *Gaia*-Sausage-Enceladus (GSE) ([Belokurov et al. 2018; Helmi et al. 2018](#)), which is linked to the last major merger that happened roughly 10 Gyr ago; the Sequoia accretion event ([Myeong et al. 2019](#)); Thamnos ([Koppelman et al. 2018](#)); Heracles, the accreted population in the inner disk ([Horta et al. 2021](#)). It has also been shown that major merger events like GSE can perturb the Galactic disk ([Belokurov et al. 2020](#)) and lead to the formation of kinematic structures like the Splash. All of these recent findings raise interest in investigating and characterizing the structures further.

The discovery of these halo substructures has raised the question of how one should select stars that come from the accreted progenitor only and avoid contamination by halo stars from other sources like the Galactic disk. For instance, [Feuillet et al. \(2020\)](#) found that to get a "clean" subset of GSE stars, one should select stars with a square root of radial actions $\sqrt{J_r} > 30$ kpc km s⁻¹. A study by [Buder et al. \(2022\)](#) shows that kinematically, GSE extends towards lower values of a square root of a radial action with a mean value around $\sqrt{J_r} \sim 26$ kpc km s⁻¹ and less than 30% of stars stay within the "clean" area. This means that purely kinematic criteria would remove a significant number of GSE stars with a lower square root of radial actions below 30 kpc km s⁻¹. Later, [Feuillet et al. \(2021\)](#) analyzed stars from the APOGEE and *Gaia* surveys and found that kinematically selected GSE and Sequoia populations contain a small number of *in situ* stars, which were identified after examining their elemental abundances.

Accreted populations stand out from the disk stars not only dynamically but also chemically, and most of them occupy partially overlapping regions in a multidimensional abundance space. For example, a study by [Contursi et al. \(2023\)](#) suggested that GSE has a higher Ce abundance than the Helmi streams, which is also an accreted population discovered by [Helmi et al. \(1999\)](#). It is known that GSE stars have lower $[\alpha/\text{Fe}]$ ratios compared to other halo stars, suggesting a different formation history (e.g. [Haywood et al. 2018](#)). Other structures, like Thamnos and Heracles, exhibit a higher $[\alpha/\text{Fe}]$ than GSE ([Horta et al. 2023](#)). In addition, [Matsuno et al. \(2021\)](#) found that GSE is enhanced in r-process elements while being under-abundant in s-process elements. The mass estimate of the GSE progenitor by [Lane et al. \(2023\)](#) is $\sim 1.45 \times 10^8 M_\odot$ and is roughly 15-25% of the Milky Way's stellar halo mass. The stellar mass of Thamnos is estimated to be $\sim 5 \times 10^6 M_\odot$ ([Koppelman et al. 2019](#)). The GSE accretion event occurred around 8-9 billion years ago, according to [Helmi et al. \(2018\)](#), while some recent studies, for instance, [Feuillet et al. \(2021\)](#) suggest a slightly older age of 10-

12 Gyr. At the time, tidal interactions between the disk and the GSE progenitor caused some of the old disk stars to gain vertical energy during the accretion event, creating a kinematically hot and physically thick disk with the same abundance pattern as the pre-interaction disk. According to [Belokurov et al. \(2020\)](#), these stars formed a kinematic structure known as the Splash.

Although so much progress has been made recently in characterizing these halo structures, many questions still need to be answered. One is whether there is any substructure within these newly discovered groups, especially in the GSE, as it is one of the largest known accreted groups to date. Answering this question would help us better understand the past and the structure of the GSE progenitor and our Galaxy. In this paper, we aim to search for kinematic structures of the stellar halo and any substructure within them and characterize their chemo-dynamical properties with the fourth data release from the GALAH survey ([Buder et al. 2025](#)).

We structure the paper in the following way. In Sect. 2, we describe the surveys used in this work and the construction of the stellar sample. In Sect. 3, we explain the methodology we used to search for structures in the stellar halo and present the main results of this work. In Sect. 4, we check how many disk stars contaminate the halo structures we identified. In Sect. 5, we discuss the chemo-dynamical properties of each group. In Sect. 6, we perform the analysis of our sample with an alternative method. We summarize the paper in Sect. 7.

2. Data

To search for and characterize substructures in the stellar halo, we need a combination of kinematic parameters and elemental abundances for thousands of stars covering a wide range of Galactocentric radii and heights above and below the plane of the Galactic disk.

In this work, we use elemental abundances and radial velocities from the GALAH survey ([De Silva et al. 2015](#)). GALAH is a high-resolution ($R \sim 28\,000$) spectroscopic survey that provides stellar parameters and elemental abundances for stars in the Southern Hemisphere. We use the GALAH Data Release 4 (hereafter GALAH DR4; [Buder et al. \(2025\)](#)), which contains almost a million stars. We combine spectroscopic data from GALAH DR4 with coordinates, parallaxes, and proper motions from the *Gaia* mission and use its latest Data Release 3 (hereafter *Gaia* DR3; [Gaia Collaboration et al. 2023](#)). The distance estimates were taken from a complementary catalog by [Bailer-Jones \(2023\)](#).

To select the most reliable elemental abundances and astrometric data for the analysis, we apply the following cuts:

1. `flag_sp == 0`
2. `snr_px_ccd3 > 30`
3. `ruwe < 1.4`
4. `survey_name = 'galah_main' or 'galah_bright' or 'galah_faint'`
5. `log g < 3.5`
6. `4000 [K] < teff < 6500 [K]`

These cuts produce the best-quality spectroscopic (cuts 1-2) and astrometric data (cut 3) and exclude open and globular clusters and other sub-surveys (cut 4). By allaying cut 1 we select stars with no identified problems with stellar parameter determination. With cut 2 we ensure to get stars with a high signal-to-noise ratio per pixel for CCD3. Cut 3 is a re-normalized unit weight error for stars and is taken from the *Gaia* DR3 catalog.

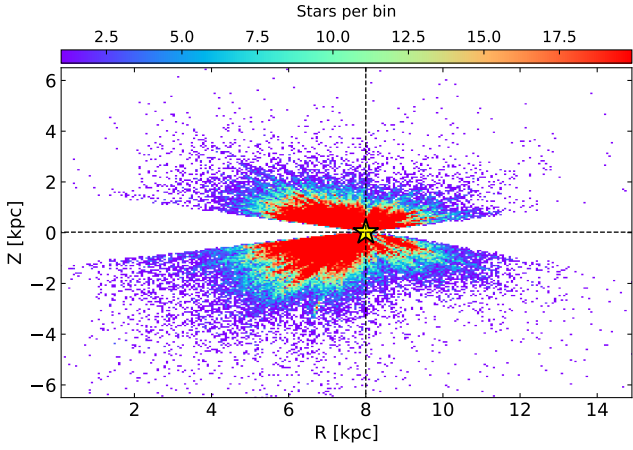


Fig. 1. Galactocentric distance, R , as a function of distance from the Galactic plane, Z , in the direction of the North Galactic Pole, $Z = 90^\circ$, for 124 618 stars selected from GALAH DR4. Dashed lines show the Solar values $R = 8$ kpc and $Z = 20.8$ pc and the yellow star shows the location of the Sun. The bin size is 0.05×0.05 kpc.

To avoid selection effects that might arise while mixing different types of stars at a wide range of Galactocentric radii, we limited our study to red giants only (cuts 5-6). Due to their long lifetime and brightness, red giants are easily observed at great distances from the Sun, allowing us to explore different parts of the Galaxy, such as the stellar halo.

As a result, we end up with a sample of 124 618 stars. Figure 1 shows the location of the selected stars in the Galactocentric cylindrical coordinate system. The Solar values of $R = 8$ kpc and $Z = 20.8$ pc and the Solar motion corrections $U_\odot = 11.1$ km s $^{-1}$, $V_\odot = 12.24$ km s $^{-1}$, and $W_\odot = 7.25$ km s $^{-1}$ were taken from Bovy (2015) and Bennett & Bovy (2019). The majority of stars can be found in the direction opposite the North Galactic Pole (NGP) and are predominantly located towards the inner Galaxy ($R \lesssim 8$ kpc). GALAH DR4 covers a broad range of Galactocentric radii and heights from the plane, allowing us to search for kinematic structures in the local stellar halo.

3. Analysis and Results

We search for kinematic structures and examine a density distribution in the $L_z - \sqrt{J_r}$ space as was used in, for example, Trick et al. (2019). We applied the wavelet transform with the *à trous* algorithm, which is an advanced statistical method described in Starck & Murtagh (2006). This method is commonly used to search for overdensities, including kinematic structures (e.g. Antoja et al. 2012; Kushniruk et al. 2017; Ramos et al. 2018). The wavelet transform has several significant advantages: no assumptions on the initial velocity distribution of stars are needed; the method allows us to detect a substructure in the sample if present at different decomposition levels proportional to the size of the structures we want to reveal.

We calculate orbital actions such as angular momenta L_z and the square root of radial actions J_r for all stars, assuming that the Galactic potential is axisymmetric. These quantities are fully conserved in axisymmetric systems and thus can be used to search for kinematic structures (Trick et al. 2019). The square root of J_r is proportional to the oscillation amplitude in the radial direction, representing the star’s epicyclic motion around its guiding radius. This relation is well illustrated in Figure 1 from Bland-Hawthorn & Tepper-García (2021). Therefore, using of

$\sqrt{J_r}$ instead of J_r is beneficial for dynamical characterization of stellar populations. To calculate actions we used the `galpy`¹ (Bovy 2015) package and the `MWPotential2014` potential. The potential consists of the Navarro-Frenk-White halo, Miyamoto-Nagai disk, and a power-law bulge available in `galpy`.

To perform the wavelet transform, we use the `PyWavelets`² package (Lee et al. 2019). Wavelet coefficients are the main characteristic of the substructure and are proportional to the intensity of their detection. The input data is a binned 2D distribution. After several tests, we found that the optimal number of bins which could provide a good balance between resolution and noise suppression for our sample was 512. The most suitable wavelet function was *Symlet 2*, as it is symmetrical and has a minimal oscillation. Among other wavelet functions, we found that Daubechies wavelet *db 2* also recovered dynamical structures well in the data, but we chose *Symlet 2* based on its highly symmetrical properties. While probing a range of decomposition steps, J , from 2 to 6, we set this parameter to five and six as it gives the best visual recovery of dynamical groups. The relation between decomposition levels, bin size, and sizes of the structures we search for is $S_J = 2^J \Delta$ (for more details, see Starck & Murtagh 2006). In our case the bin size, Δ , for 512 bins is $[\sqrt{J_r}, L_z] \simeq [0.2, 11.7]$ kpc km s $^{-1}$. Thus, for scale $J = 6$, we search for structures with sizes $[\sqrt{J_r}, L_z] \simeq [12.8, 748]$ kpc km s $^{-1}$, and similarly for the scale $J = 5$ we recover structures with sizes $[\sqrt{J_r}, L_z] \simeq [6.4, 374]$ kpc km s $^{-1}$.

Panel (a) of Figure 2 shows the initial 2D distribution of all 124 618 stars in the $L_z - \sqrt{J_r}$ space. The Galactic disk is a dominant part of our sample and is seen at $\sqrt{J_r} < 20$ kpc km s $^{-1}$ and $L_z > 1000$ kpc km s $^{-1}$. The halo part accounts for fewer stars but is clearly visible in the sample.

As the next step, we generate 500 Monte Carlo $L_z - \sqrt{J_r}$ maps of the initial 2D distribution, shown in panel (a) of Figure 2 to which we apply the wavelet transform. This step is needed to check the significance of the detected overdensities. We calculated a covariance matrix between the parameters and found that most correlation coefficients are close to zero, indicating an insignificant dependence. Thus, we assume that a star’s radial velocity, coordinates, proper motions, and distances follow a Gaussian distribution from which we draw values randomly and recalculate $L_z - \sqrt{J_r}$ 500 times. The mean values and widths of the Gaussian distributions are defined by the measured values and their corresponding uncertainties taken from the initial sample. Then, the wavelet transform is applied to every Monte Carlo-generated sample, and the central positions of all detected structures are over-plotted. Performing Monte Carlo simulations allows us to estimate the sizes and uncertainties of the detected kinematic groups. We found that 500 Monte Carlo-generated samples are enough to converge the results.

The resulting wavelet transform maps for scales $J = 5$ and $J = 6$ are shown in panels (c) and (c) of Figure 2 respectively. Both plots show sums of the wavelet transform maps of all 500 Monte Carlo-generated samples. With the help of an image processing package for Python called `scikit-image`³ (van der Walt et al. 2014) and its peak detection algorithm, we found seven overdensities for scale $J = 5$ and two overdensities for scale $J = 6$, which are marked with white crosses. Based on comparison of the results with the literature (e.g. Koppelman et al. 2018; Feuillet et al. 2020; Horta et al. 2021) the disk, Splash, GSE (two crosses above $\sqrt{J_r} > 20$ kpc km s $^{-1}$), Tham-

¹ <http://github.com/jobovy/galpy>

² <https://pywavelets.readthedocs.io>

³ <https://scikit-image.org>

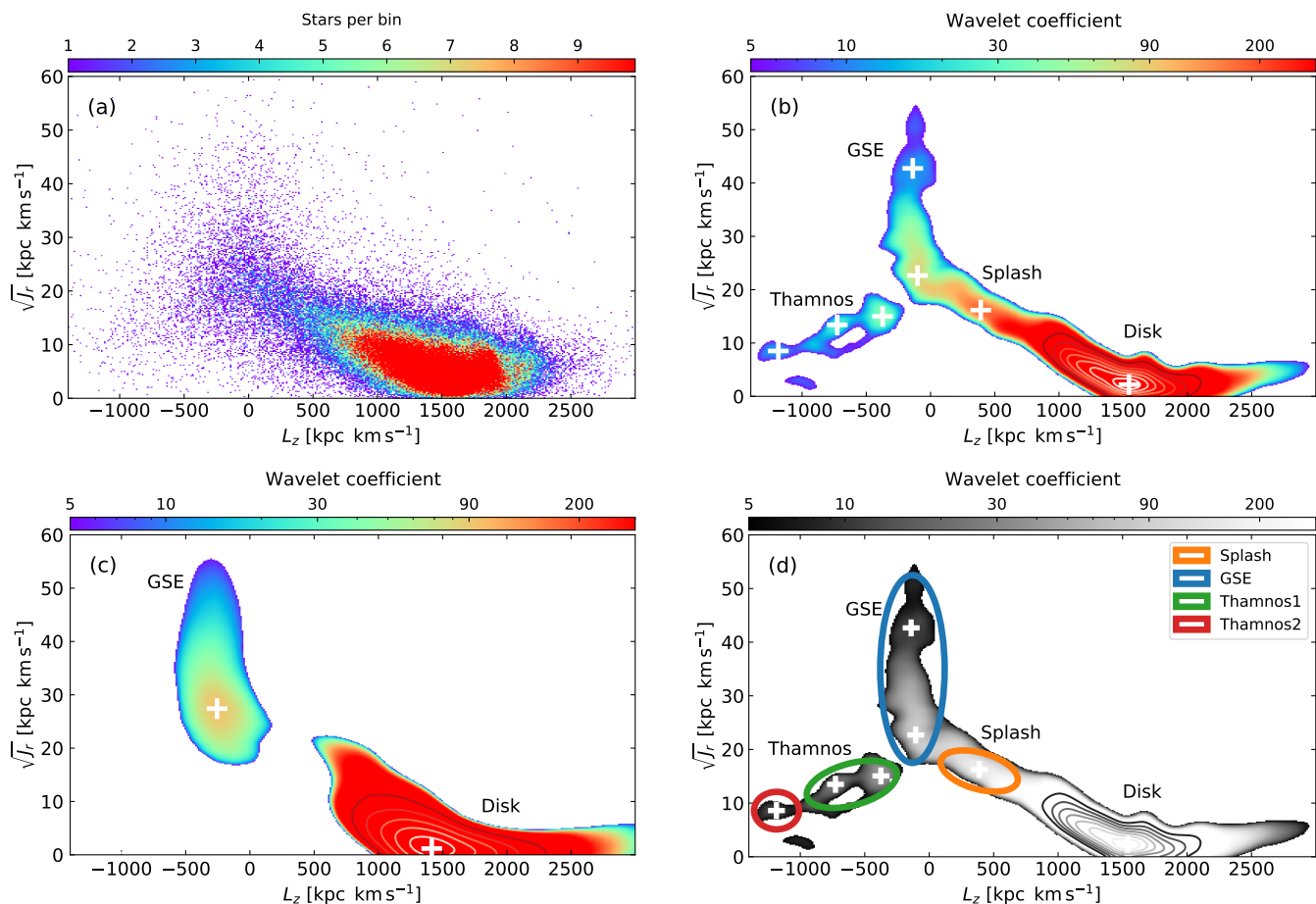


Fig. 2. Panel (a): Density map in $L_z - \sqrt{J_r}$ space of 124 618 stars that were selected from GALAH DR4. The bin size is 11.7×0.2 kpc km s $^{-1}$. Panel (b): The wavelet transform map of 500 Monte-Carlo-generated samples in the $L_z - \sqrt{J_r}$ space for scale $J = 5$. Centres of the detected structures are shown with white crosses. The structures are the disk, Splash, GSE, and Thamnos. Panel (c): The wavelet transform map of 500 Monte-Carlo-generated samples in the $L_z - \sqrt{J_r}$ space for scale $J = 6$. Centres of the detected structures are shown with white crosses. GSE and the disk are the two main building blocks. Panel (d): The same as panel (b), but in a gray scale. The ellipses show areas in the $L_z - \sqrt{J_r}$ space where we select stars to further analyze the detected kinematic structures.

Table 1. Detected kinematic structures identified in this work.

Group	$\sqrt{J_r} \pm \delta$ [kpc km s $^{-1}$]	$L_z \pm \delta$ [kpc km s $^{-1}$]	Number of stars
Splash	16.0 ± 4.5	388 ± 300	3 071
GSE	35.0 ± 17.5	-130 ± 250	1 895
Thamnos1	13.5 ± 4.0	-600 ± 350	413
Thamnos2	8.6 ± 3.5	-1184 ± 175	29

Notes. Names of the structures are listed in Col. 1. Cols. 2 and 3 give the centres of the ellipses drawn around the kinematic structures, from which stars were selected for further analysis (see Fig. 2, panel d). The half-widths and half-heights of the ellipses (δ) are given in Cols. 2 and 3. Col. 4 provides the number of stars in each group.

nos1, and Thamnos2 can be easily recognized based on their location on the $L_z - \sqrt{J_r}$ map. We found that GSE consists of two peaks on a scale of $J = 5$, while Thamnos has three peaks that we distil into Thamnos1 and Thamnos2 groups based on previous studies. Next, we draw ellipses around the crosses as shown on panel (d) of Figure 2 and select stars inside the ellipses to further analyze the detected kinematic structures. The ellipses were drawn based on a visual inspection of the struc-

tures, with a comparison of the resulting wavelet space to existing findings in the literature. Centers of the ellipses, widths and heights, and the number of stars inside each group we provide in Tab. 1. The biggest ellipse belongs to GSE, for which we combined two peaks in scale $J = 5$ as the structure is seen as a whole in scale $J = 6$. We selected the most significant number of stars in the Splash population compared to the other groups. This reflects the dominance of the Solar neighborhood in the GALAH survey data.

4. Contamination of the structures from the disk and halo

In recent studies, such as those conducted by Feuillet et al. (2021), Horta et al. (2023), and Feltzing & Feuillet (2023), it was demonstrated that even though the kinematic and dynamical selection is efficient in identifying accreted halo populations, some "in situ" stars can still be included in the resulting sample. We check fractions of stars that belong to the chemically defined disk and halo in the total sample. To split stars into the disk and halo populations, we follow the approach used in Buder et al. (2021) and study the distribution of stars in the [Mg/Cu] versus [Na/Fe] space. [Mg/Cu] is a tracer of SNe II contributions from massive stars and SNIa of low-mass stars (Kobayashi et al.

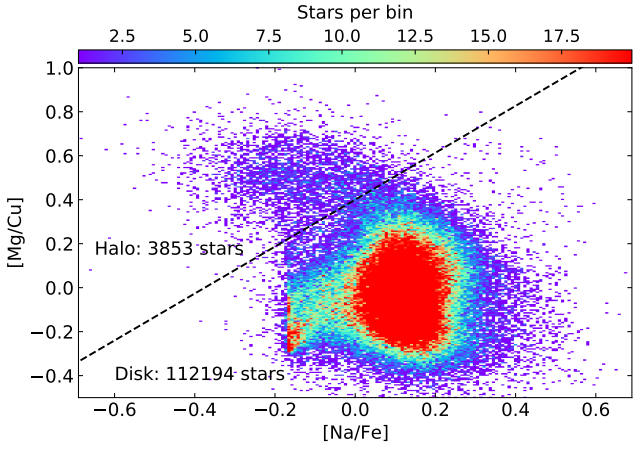


Fig. 3. The binned distributions of 116 047 stars selected from the GALAH DR4 in the $[Mg/Cu] - [Na/Fe]$ plane. The bin size is 0.01×0.01 . The dashed line shows the division of stars into the disk (below the line) and halo (above the line) stars.

2020). Similarly to $[Mg/Fe]$, $[Na/Fe]$ allows tracking differences between the *in situ* and accreted stars (e.g. Nissen & Schuster 2010).

We also selected stars for which there are no identified problems with abundance determination of a chemical element X by setting the flag `flag_X_fe` to zero. We applied this flag to each of the earlier-mentioned chemical elements to avoid inaccuracies in the analysis. The flags are given in the GALAH DR4 survey. Applying the flags to Mg, Cu, Na, and Fe abundances reduces the sample to 116 047 stars. Figure 3 shows the fractions of stars belonging to the disk population (below the dashed line) and the halo (above the dashed line). The dashed line was visually determined after examining the density distribution. Figure 4 shows the sample of 116 047 GALAH stars in gray and the different colors and shapes show stars in the Splash, GSE, Thamnos1, and Thamnos2 structures. Some stars in the disk population are found to fall into the part of the plot around $[Na/Fe] \approx -0.17$, which is merely an artefact of the GALAH spectroscopic analysis pipeline. However, despite this, we do not exclude them from the study as most of these stars still belong to the disk population rather than the halo. Below, we discuss contamination fractions for each of the detected kinematic structures.

- Splash. By its definition, the Splash should be composed of stars with disk-like chemistry that were brought to halo-like orbits by the last major merger event (see Belokurov et al. 2018). According to this definition, we found that $\approx 86\%$ of stars in the group we found can be categorized as chemically belonging to the disk, while the remaining $\approx 14\%$ exhibit chemical characteristics associated with the halo.
- GSE. The GSE population originates from the last merger event and consists of accreted stars from the satellite Enceladus (Helmi et al. 2018). Thus, GSE stars are expected to be chemically distinct from the disk stars. Panel (b) of Figure 4 shows that $\approx 57\%$ stars in the group we link to the GSE belong to the stellar halo, while the contamination from the disk is $\approx 43\%$.
- Thamnos1. Thamnos1 is also believed to be a remnant of an accretion event and, thus, chemically differentiable from the disk (Koppelman et al. 2019). In the plot on panel (c) of Figure 4, we see that the contamination from the disk is $\approx 55\%$, and there is only $\approx 45\%$ of halo stars.

Table 2. KDE metallicity peak values for the detected kinematic structures.

Group	$[Fe/H]_{\text{peak}}$	$\delta[Fe/H]$	Number of stars
Splash	-0.55	0.04	2 200
GSE	-1.20	0.07	748
Thamnos1	-1.17	0.18	134
Thamnos2	-1.28	0.79	7

Notes. The peak metallicity ($[Fe/H]_{\text{peak}}$), corresponding uncertainties ($\delta[Fe/H]$), and the number of stars are listed for each kinematic group.

- Thamnos2. Similarly to Thamnos1, Thamnos2 is expected to be clean from the disk stars. Panel (d) of Figure 4 shows that $\approx 88\%$ of the stars belong to the halo, and only one object is a disk star ($\approx 12\%$).

Taking into account the definitions of the aforementioned kinematic structures and their contamination fractions, which are shown in Figure 4, we decided to exclude chemically-defined halo stars from the Splash and chemically-defined disk stars from the remaining four groups.

Figure 5 shows the orbital energy distribution as a function of angular momentum and the rotational velocity versus metallicity for the entire sample and the kinematic structures detected. The results we observe agree with other studies that investigated similar distributions like Koppelman et al. (2019) and Belokurov et al. (2018). The Splash is a connection between the Galactic disk stars and halo populations. The minor difference that we observe is that although stars in the GSE (Galactic substructure) population are close to $L_z \approx 0 \text{ kpc km s}^{-1}$, they tend to follow slightly more retrograde orbits than prograde ones.

5. Chemo-dynamical characterization of the groups

Figure 6 shows normalized metallicity distributions and corresponding uncertainties for the detected kinematic structures. These distributions were derived using kernel density estimation (KDE) algorithms from the `scikit-learn`⁴ package (Pedregosa et al. 2011). Contamination of the halo and disk was removed for the Splash and the rest of the groups, respectively (see Sect.4). Table 2 provides metallicity values, $[Fe/H]$, where the normalized probability density has a maximum value and corresponding uncertainties, δ . All groups have wide metallicity distributions and distributions of Galactocentric radii. Thamnos1 and Thamnos2 appear to have multiple-peaked distributions. This could be due to potential substructure within the groups or remaining contamination of the structures by field stars. GSE is the structure that covers the broadest range of Galactocentric radii and goes in the outer Galaxy ($R \gtrsim 8 \text{ kpc}$). The metallicity distribution of the GSE peaks at ≈ -1.2 and is in agreement with other studies like Naidu et al. (2020), who found a value of ≈ -1.2 , and Feuillet et al. (2021), who found a mean value of ≈ -1.15 . The peak of the metallicity distribution of Splash is ≈ -0.6 , which is in agreement with, for example, Belokurov et al. (2020) and Sanders et al. (2021). However, Thamnos1 and Thamnos2 have mean metallicities ≈ -1.4 according to Bellazzini et al. (2023), whereas, in our study, we found the peak of the metallicity distribution at ≈ -1.2 for Thamnos1 and ≈ -1.3 for Thamnos2, although these differences are still within the errors.

⁴ <https://scikit-learn.org/>

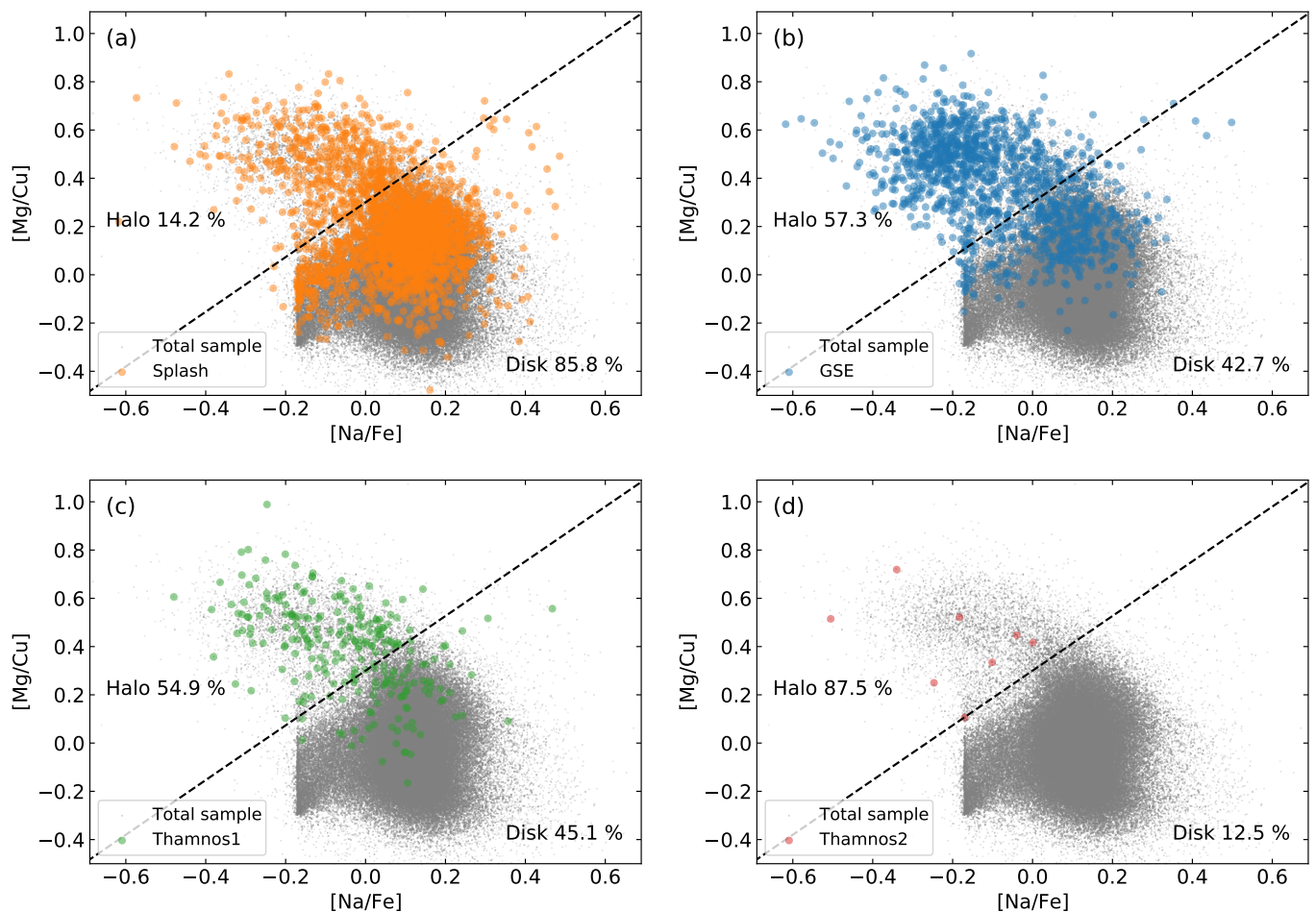


Fig. 4. A scatter plot of all 116047 stars selected from GALAH DR4 in the $[Mg/Cu] - [Na/Fe]$ plane is shown in gray. The markers of different colors show stars in the following kinematic structures: Splash (Panel (a), orange circles), GSE (Panel (b), blue circles), Thamnos1 (Panel (c), green circles), and Thamnos2 (Panel (d), red circles). The dashed line is the same as on panel (a) and divides the stars into the disk and halo sub-samples. Percentages of the halo and disk stars in the kinematic structures are provided in each plot.

Figure 7 shows individual distributions of elemental abundances of all five kinematic structures, which are presented as box plots for 32 chemical elements. We included only stars for which individual elemental abundance flags, $flag_X_fe = 0$, to get the most precise data for the box plots. Note that Mg, Fe, Cu, and Na abundances were used to identify populations, which means that we cannot draw purely independent conclusions based on these chemical elements.

Figure 8 shows a more detailed view of several elemental abundance spaces, such as $[Mg/Fe]$, $[Ba/Fe]$, and $[Ba/Mg]$ as a function of metallicity. All of these chemical spaces provide details about the star formation history of the detected kinematic groups, as all of these chemical elements have different origins. The running means of the detected structures are shown as colored lines, and the corresponding errors are shown as shaded regions. These shaded regions represent the standard error of the mean within each running window, calculated from the individual abundance uncertainties of the stars in that window. The total sample is shown in the background as gray dots for comparison. The window size for the running means was estimated based on the number of stars in each kinematic group and ranges from 5 to 50. The step size was adopted as half the window size. Since Thamnos2 has very few stars for the running means we show them as a scatter plot.

The uneven running mean of Thamnos1 results from several factors. Firstly, Thamnos1 has fewer identified stars compared to GSE and Splash. Secondly, the spike in Thamnos1 in panels (b) and (c) of Fig. 8 is likely due to contamination in the sample. This further emphasized the importance of combining both dynamical and chemical parameters to obtain the purest sample possible.

Below, we discuss elemental abundance patterns of each of the detected kinematic structures based on Figures 7 and 8.

- The abundance of α -elements such as C, O, Ca, Mg, Al, Si, and Ti are slightly higher in the halo structures. This is especially noticeable for Thamnos2, whose oxygen abundance is higher than that of the rest of the groups. This result is in agreement with [Horta et al. \(2023\)](#), who showed that Thamnos shows a higher $[\alpha/Fe]$ ratio than the other halo substructures.
- Iron-peak elements, including Co, Cr, Fe, Mn, Ni, Sc, and V, show different behaviours. Co, Fe, Ni, Sc, and V are more abundant in Splash than in the halo structures. The distributions of Cr and Mn are monotonic and do not vary between the groups. [Sanders et al. \(2021\)](#) and later [Nissen et al. \(2024\)](#) studied iron-peak abundances in the accreted halo populations and found low abundances of $[Ni/Fe]$. We

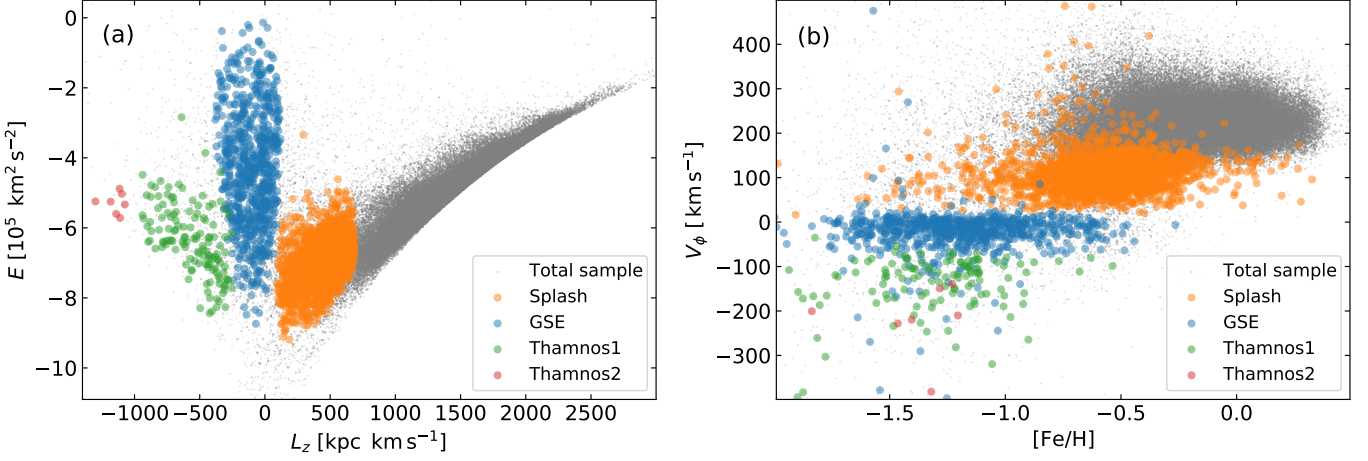


Fig. 5. Panel (a): The plot shows the orbital energy as a function of the angular momentum. Gray dots show a scatter plot of the total sample, and other colors and symbols correspond to the kinematic structures detected in the legend. Chemically-defined halo stars were excluded from the Splash, and chemically-defined disk stars were excluded from the rest of the groups. Panel (b): Similar to the plot on panel (a), but showing the rotational velocity as a function of metallicity.

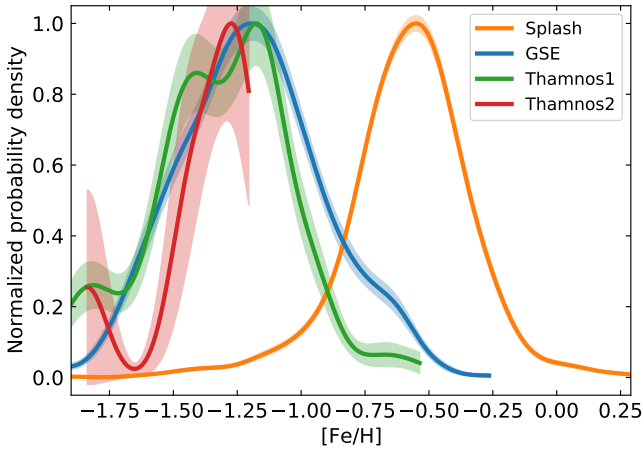


Fig. 6. Normalized probability density metallicity $[Fe/H]$ with uncertainty bands for kinematic groups listed in the legend. The chemically-defined halo stars were excluded from the Splash, and chemically-defined disk stars were excluded from the rest of the groups. The plot is generated using kernel density estimation (KDE) with a bandwidth of 0.075 and Gaussian kernel. The shaded regions around each curve represent corresponding uncertainties, which are standard deviations of 100 bootstrap samples.

observe a minor under-abundance of $[Ni/Fe]$ in the accreted populations compared to Splash.

- Typical s-process (slow neutron-capture process) elements such as Ba, Ce, La, Mo, Nd, Rb, Sr, Y, and Zr are abundant in the accreted populations. The exception is Rb, whose abundance is lower for GSE than the rest of the structures, and Sr, for which very few stars in the structures have measurements. Thus, there are insufficient statistics for a proper analysis. However, [Matsuno et al. \(2021\)](#) found a contribution of r-process elements dominates over s-process. This is in agreement with our results for other s-process elements in GSE like Ba (see Fig. 8). The abundance of Ce, an s-process element, is much higher in GSE than in Splash, which contradicts the idea of low s-process abundances in GSE. [Conrursi et al. \(2023\)](#) found that Thamnos and GSE have sim-

- ilar Ce abundance, while our box plots show that GSE and Thamnos2 have a slightly lower median than Thamnos1.
- GALAH DR4 provides abundances of the following r-process (rapid neutron-capture process) elements: Eu, Nd, and Sm. Eu is not used here due to its current unreliability in DR4. GSE tends to have a higher abundance of r-process elements than other structures. This result is also in agreement with previous findings on GSE ([Matsuno et al. 2021](#)).
- The abundance of Cu, Ru, and Zn, elements produced by explosive and non-explosive nucleosynthesis, show different patterns. Copper is more abundant in Splash than the halo groups and is likely because we chemically defined disk and halo groups using Cu abundance (see Sect.4). The abundance of Ruthenium is higher for GSE than Splash and Thamnos1. Zn is slightly more abundant in Thamnos1 and Thamnos2.
- Abundances of K and Na, elements primarily produced through nucleosynthesis in stars. Both elements are slightly more abundant in the halo structures, although we used Na abundance to divide samples into the chemically defined disk and halo.
- Halo structures are more abundant in Li compared to Splash. The abundance of lithium in GSE was studied, for example, by [Molaro et al. \(2020\)](#) and [Simpson et al. \(2021\)](#). It was shown that The $A(Li)$ abundances versus $[Fe/H]$ in the GSE population behave similarly to *in situ* stars, especially at low metallicities.
- The $[Mg/Fe]$ – $[Fe/H]$ space (see panel (a) in Fig. 8) shows a negative slope for all groups, reflecting the overall decline of α -element abundances with increasing metallicity. The Splash occupies the thick disk region of the distribution, while GSE exhibits lower $[Mg/Fe]$ values than both the Splash and Thamnos1. Thamnos1 follows a trend very similar to the Splash, indicating a later α -knee and more efficient chemical enrichment. We note that possible contamination in the Thamnos1 selection may blur this trend. This behaviour is consistent with Thamnos1 having experienced more rapid star formation than GSE and is in agreement with, for example, [Horta et al. \(2021\)](#), who explored the chemical properties of kinematic substructures using the APOGEE survey.
- Thamnos1 and GSE show similar behavior in the $[Ba/Fe]$ – $[Fe/H]$ and $[Ba/Mg]$ – $[Fe/H]$ spaces (see panels (b), and (c) in Fig. 8), with both showing increasing trends with

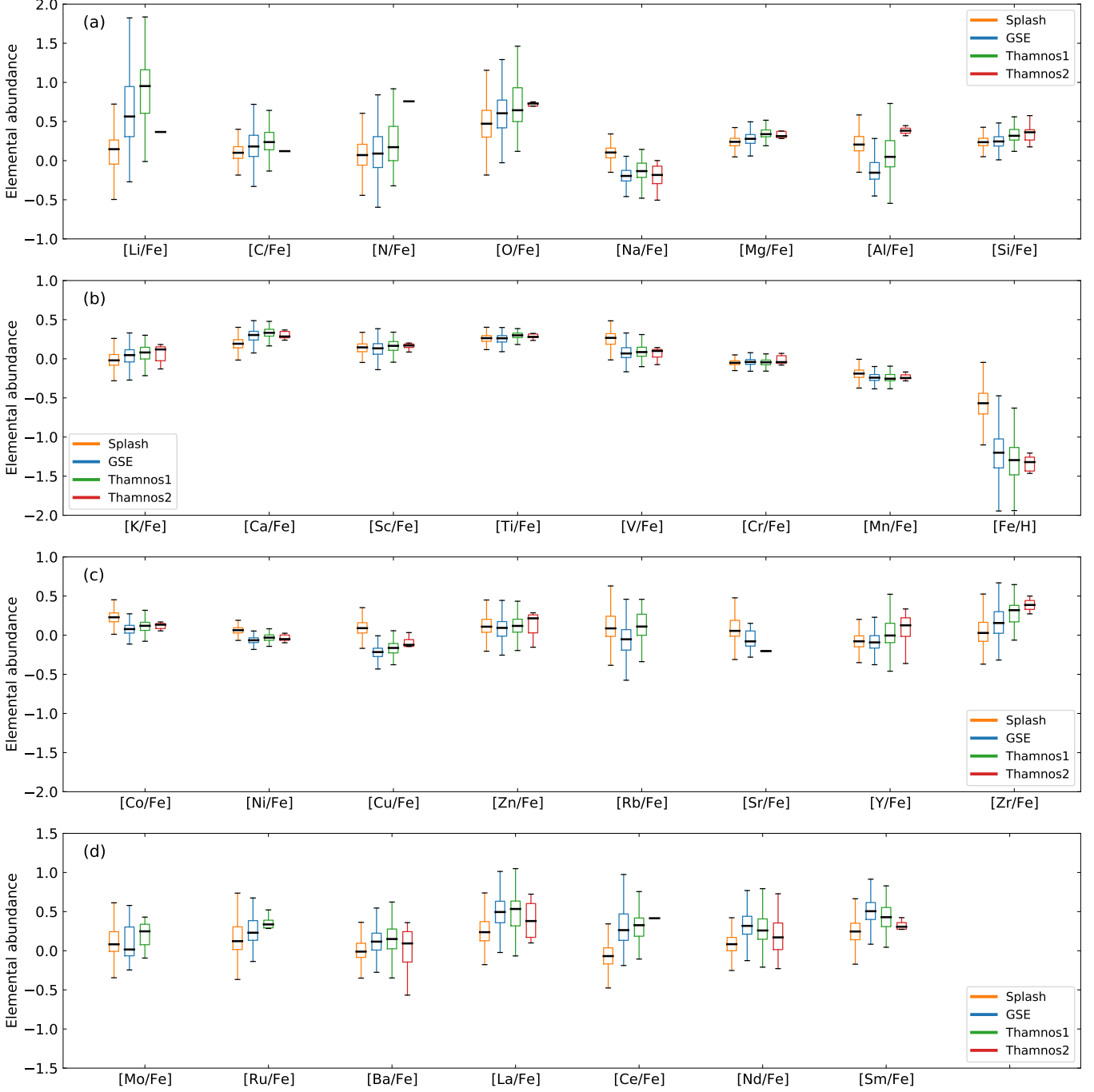


Fig. 7. Panels (a) – (d) show individual distributions of elemental abundances for the Splash (orange box), GSE (blue box), Thamnos1 (green box), and Thamnos2 (red box) are depicted using box plots. The analysis covers 32 chemical elements, X, related to iron, $[X/Fe]$, and iron abundance, which is related to hydrogen, $[Fe/H]$. Each box plot adheres to standard conventions, with the first and third quartiles defining the box body, "whiskers" extending to minimum and maximum values, and the median shown as a black line inside each box.

metallicity. The slope is steeper for Thamnos1 than for GSE, consistent with more rapid star formation and a stronger delayed contribution from AGB stars. The Splash exhibits a shallower slope, more similar to GSE, indicating that Thamnos1 may have undergone a chemical evolution different from both the Milky Way and GSE. We note that contamination and small number statistics may affect the precise slopes, but the overall trend is consistent with faster enrichment for Thamnos1.

Overall, accreted halo populations are chemically different from the disk stars. We also observed differences in elemental abundances among the dynamical populations, confirming that these groups have an extragalactic origin. Although the conclusion is, however, influenced by our chemical grouping, performing chemical, dynamical, and kinematic selection together is essential to neatly selecting stars that belong to the accreted groups.

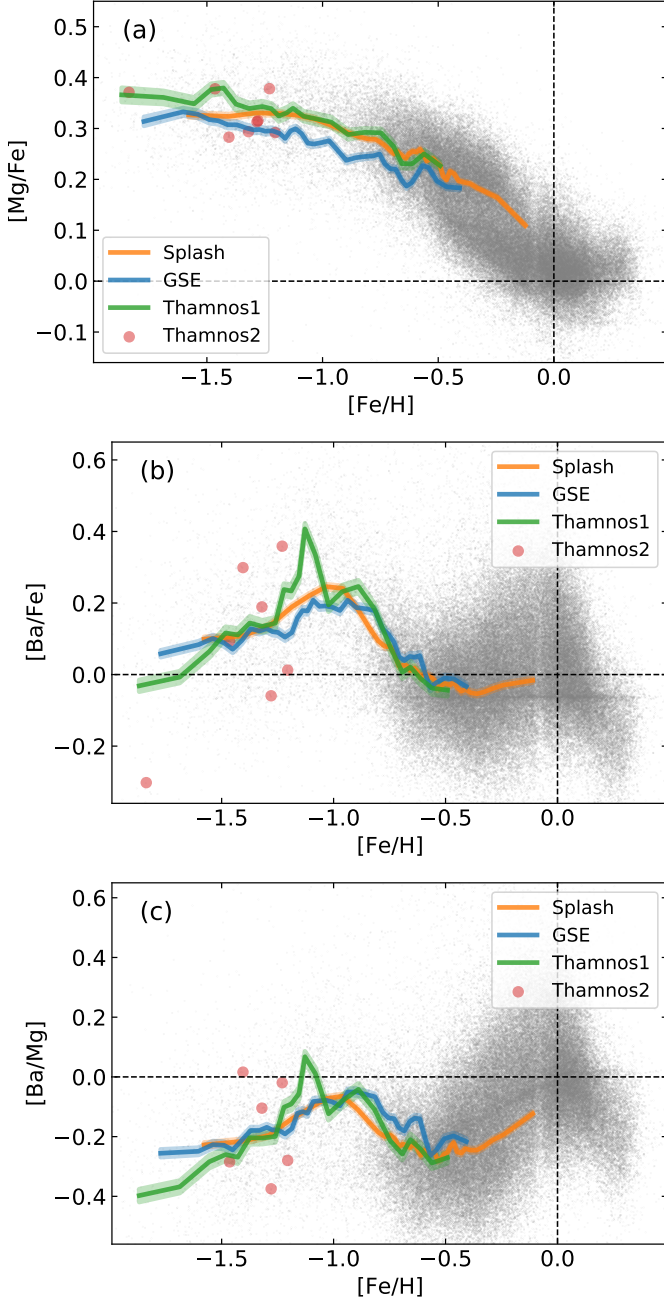


Fig. 8. Distribution of stars selected from GALAH DR4 in the following elemental abundance planes: (a) $[\text{Mg}/\text{Fe}] - [\text{Fe}/\text{H}]$, (b) $[\text{Ba}/\text{Fe}] - [\text{Fe}/\text{H}]$, (c) $[\text{Ba}/\text{Mg}] - [\text{Fe}/\text{H}]$. The gray dots represent the total sample, while the colored lines show running means with shaded error regions for stars from kinematic structures as labeled in the legend. Stars in Thamnos2 are shown as dots due to the low number of stars in the group. The dashed lines indicate where the x- and y-axis are equal to zero.

6. Chemo-dynamical tagging of the accreted structures with t-SNE

Given that both dynamics and chemistry are essential for selecting halo substructures, we also investigate a method of selecting the halo substructures based solely on chemistry, in order to complement the dynamical selection using wavelets. To accomplish this, we use the algorithm t-distributed stochastic neighbor embedding (t-SNE), which implements dimensionality reduction based on non-linear manifold learning (Hinton & Roweis

2002; van der Maaten & Hinton 2008). Kos et al. (2018) showed the efficiency of this algorithm for identifying ejected stars from star clusters using chemical tagging with GALAH data, identifying two ejected stars several degrees from the main body of the Pleiades open cluster. A follow-up study by Youakim et al. (2023) combined both chemistry and kinematics from GALAH data, using 20 parameters as input into t-SNE and found several tidally stripped stars from Omega Centauri, thereby constraining the cluster’s initial mass and evolution time in the Galaxy. In another recent study conducted by Ortigoza-Urdaneta et al. (2023), the t-SNE algorithm was used to investigate chemical structures in a sample of 1 742 red giants with rotational velocity $V_\phi < 100 \text{ km s}^{-1}$. The sample was selected from the APOGEE DR17 (Abdurro’uf et al. 2022) and *Gaia* surveys. The input parameters of the t-SNE analysis included elemental abundances of 10 chemical elements. As a result of their study, they identified the GSE and Splash populations, as well as a few new structures. Taken together, these results demonstrate that the t-SNE algorithm is a helpful tool for grouping stars based on their chemical properties.

As input for the t-SNE algorithm in this study, we included measured abundances of 15 chemical elements: $[\text{Fe}/\text{H}]$, $[\text{O}/\text{Fe}]$, $[\text{Na}/\text{Fe}]$, $[\text{Mg}/\text{Fe}]$, $[\text{Al}/\text{Fe}]$, $[\text{Si}/\text{Fe}]$, $[\text{K}/\text{Fe}]$, $[\text{Ca}/\text{Fe}]$, $[\text{Sc}/\text{Fe}]$, $[\text{Cr}/\text{Fe}]$, $[\text{Mn}/\text{Fe}]$, $[\text{Y}/\text{Fe}]$, $[\text{Ba}/\text{Fe}]$, and $[\text{Cu}/\text{Fe}]$. After application of the quality flags for each of these elements (`flag_x_fe = 0`), as well as removal of any star missing data for any of these abundances (we only included measurements, not upper limits), the sample was reduced to 107 769 stars.

In order to mitigate the different ranges of these abundances, we standardized each input distribution such that they were transformed to have a median of 0 and a standard deviation of 1. In practice, we accomplished this by subtracting each abundance value from the median and dividing by the standard deviation. The abundance distributions are close enough to being Gaussian that this simple standardization was sufficient. We also applied weights in order to increase the contribution from certain abundances. Weights for abundances were selected to increase the contribution of elements that are known from the literature to be important for selecting halo substructures, such as $[\text{Fe}/\text{H}]$ and $[\text{Cu}/\text{Fe}]$, and to account for the observational uncertainties, where the weights of abundances with large observational uncertainties are reduced. A thorough investigation of the weights for different abundances in GALAH was conducted in Kos et al. (2018), and we refer the reader there for a more detailed description. In this work, we adopt the weights used in that paper, and all of the weights for the input parameters are summarized in Table 3. We also checked the analysis using uniform weights, and found that the structures were still localized in the latent space, but with a slightly higher contamination.

The middle panel of Figure 9 shows the two-dimensional latent space projection resulting from the dimensionality reduction. There are two input hyper-parameters that we used to initiate the t-SNE, `n_jobs`, which defines how many CPU cores are dedicated for the computation and for which we used a value of 4, and `perplexity`, which is a measure of the expected size of the groups that cluster in the latent space. Lower perplexity values allow to highlight smaller groups, while higher values help to detect large-scale structure. After probing a range of values, we chose a perplexity of 1 000 as input into the algorithm. Smaller values tended to separate the labeled GSE stars into several smaller substructures, and values much larger than this resulted in a single uniform cluster of all of the stars in the sample. The filled colored points show the selected stars using the wavelet analysis, limited to candidates that are also consis-

Table 3. List of all of the weights used for the standardized input t-SNE parameters.

Param	Weight	Param	Weight	Param	Weight
O	1.0	Ti	2.0	Ca	0.5
Na	1.0	Cr	2.0	Y	0.25
Mg	0.50	Mn	1.0	Sc	1.0
Al	1.0	Fe	2.0	Ba	0.25
K	0.25	Cu	2.0	Si	1.0

tent with being halo stars for GSE and Thamnos, and limited to disk stars for the Splash (open circles are the disk stars that were removed according to the selection shown in Figure 4). Stars selected as GSE stars in the wavelet analysis (blue points) cluster very tightly in the t-SNE projection, demonstrating that these can be identified from field stars and disk stars based solely on their elemental abundance patterns. However, the GSE stars overlap substantially with the Thamnos1 and Thamnos2 stars (green and red points), suggesting that they are not chemically distinct enough, or that the GALAH abundances are not precise enough, to differentiate these structures through chemical tagging alone. The blue and green open circles which scatter up the bottom half of the t-SNE map indicate that the cut made to select halo stars in Figure 4 is very effective at removing contaminants from a purely kinematic selection.

Surrounding the main t-SNE latent space projection in Figure 9, there are smaller representations of the same latent space, but color coded by different parameters. This is very insightful to see which abundances are the most important in the identification of these halo substructures. We note that we have not plotted the maps for [K/Fe] and [Y/Fe], since both of these were very uniform and contained little information, with [Y/Fe] looking exactly the same as [Ba/Fe], since these elements share similar chemical evolutionary pathways. Instead, we include the dynamical parameters $\sqrt{J_r}$, J_z and L_z , which were not included as inputs into the t-SNE. Notable elements include [Fe/H], with a clear metallicity gradient showing in the latent space, [Cu/Fe], as well as alpha elements [Mg/Fe], [Ca/Fe], [Ti/Fe], and the light elements [Na/Fe] and [Al/Fe], all of which previously have been shown to be important tracers in Galactic chemical evolution. Finally, all of the dynamical parameters $\sqrt{J_r}$, J_z and L_z show a clearly visible feature at the location of GSE and Thamnos in the latent space, confirming that there is a distinct overlap in the chemical and kinematic signatures of these structures.

We note that there are several other obvious overdensities located in the disk stars shown in gray in Figure 9. We investigated these and found that most of them are kinematic moving groups in the disk, like Hercules, Sirius, Coma Berenices, Pleiades, Hyades and others, that have previously been discussed in the literature (ex.: Antoja et al. 2012; Ramos et al. 2018; Kushniruk et al. 2017; Kushniruk & Bensby 2019) or some remnants of globular cluster stars in the outskirts of the cluster that were not removed by the selection criteria. A proper analysis of these structures is beyond the scope of this paper, but demonstrates the efficiency of t-SNE at identifying chemical structures in the Galaxy.

7. Summary

In this work, we analyzed a sample of 124 618 carefully selected red giants from the GALAH DR4 and *Gaia* surveys using

wavelet transform and t-SNE algorithms. Our analysis revealed the following:

- Using the wavelet transform technique, we were able to detect the main structures of a space defined by a square root of radial action and angular momentum, namely the Galactic disk, Splash, GSE, Thamnos1 and Thamnos2.
- The strongest detection in the wavelet maps corresponds to the Galactic disk. This is due to a large number of disk stars (112 194) in our sample. The t-SNE algorithm revealed dozens of disk structures, among which we could recognize well-known moving groups in the Galactic disk.
- The Splash population on the wavelet transform map plays the role of a bridge that links the metal-rich part of the Galactic disk and GSE. Because of proximity to accreted populations in action space, these *in situ* stars on halo-like orbits contaminate them if selected purely based on kinematics. On the other hand, the Splash population is also contaminated by the halo stars. We observe only one peak that we link to Splash.
- Our findings indicate that GSE can be divided into two substructures: the blob of accreted stars at $J_r > 40$ kpc km s⁻¹ and the blob at lower values of the square root of the radial action, which is a mixture of *in situ* and accreted stars. We also observe that the GSE population is not purely a non-rotating component of the Galaxy. Wavelet transform shows that although close to $L_z \approx 0$ kpc km s⁻¹, many stars follow slightly retrograde orbits.
- In Thamnos, we discovered three peaks in the action space. Two of these peaks are combined and referred to as the Thamnos1 group. A kinematic selection of stars in the Thamnos1 group indicates that a substantial number of them belong to the high-alpha disk. However, these stars can be removed from the sample if the elemental abundances of individual stars are studied. Thamnos2, on the other hand, is mainly composed of halo stars.
- The analysis of our sample with the t-SNE method using only chemical abundances as input successfully recovers the groups of stars identified with the wavelet transform. Chemical tagging could differentiate GSE, Thamnos1 and Thamnos2 from the bulk Milky Way population, but could not separate these halo structures from each other based on chemistry alone. This indicates the importance of kinematics for identifying and separating differentiating these structures. The t-SNE analysis also showed that the halo selection in [Mg/Cu] vs. [Na/Fe] space is very effective at removing contamination when selecting stars in GSE, Thamnos1 and Thamnos2. The splashed disk is located in immediate proximity to the accreted group of stars, indicating that the Splash contaminates the selection of accreted populations.

The analysis of chemical properties of the stars in the kinematic groups is partly influenced by the way we defined the groups chemically based on Mg, Fe, Cu and Na elemental abundances, but still allows us to conclude the following:

- Although a kinematic selection only allows the choice of stars in the accreted populations, an analysis of the chemical properties of these stars is needed for the ‘purest’ selection. The structures close to the L_z and with $\sqrt{J_r} < 25$ kpc km s⁻¹ have a higher contamination rate.
- The peak values of metallicity distributions for each group are in agreement with the previous studies and place Splash at -0.6 dex, GSE at -1.2 dex, Thamnos1 at -1.2, Thamnos2 at -1.3 dex. Peaks of the Galactocentric radius distributions

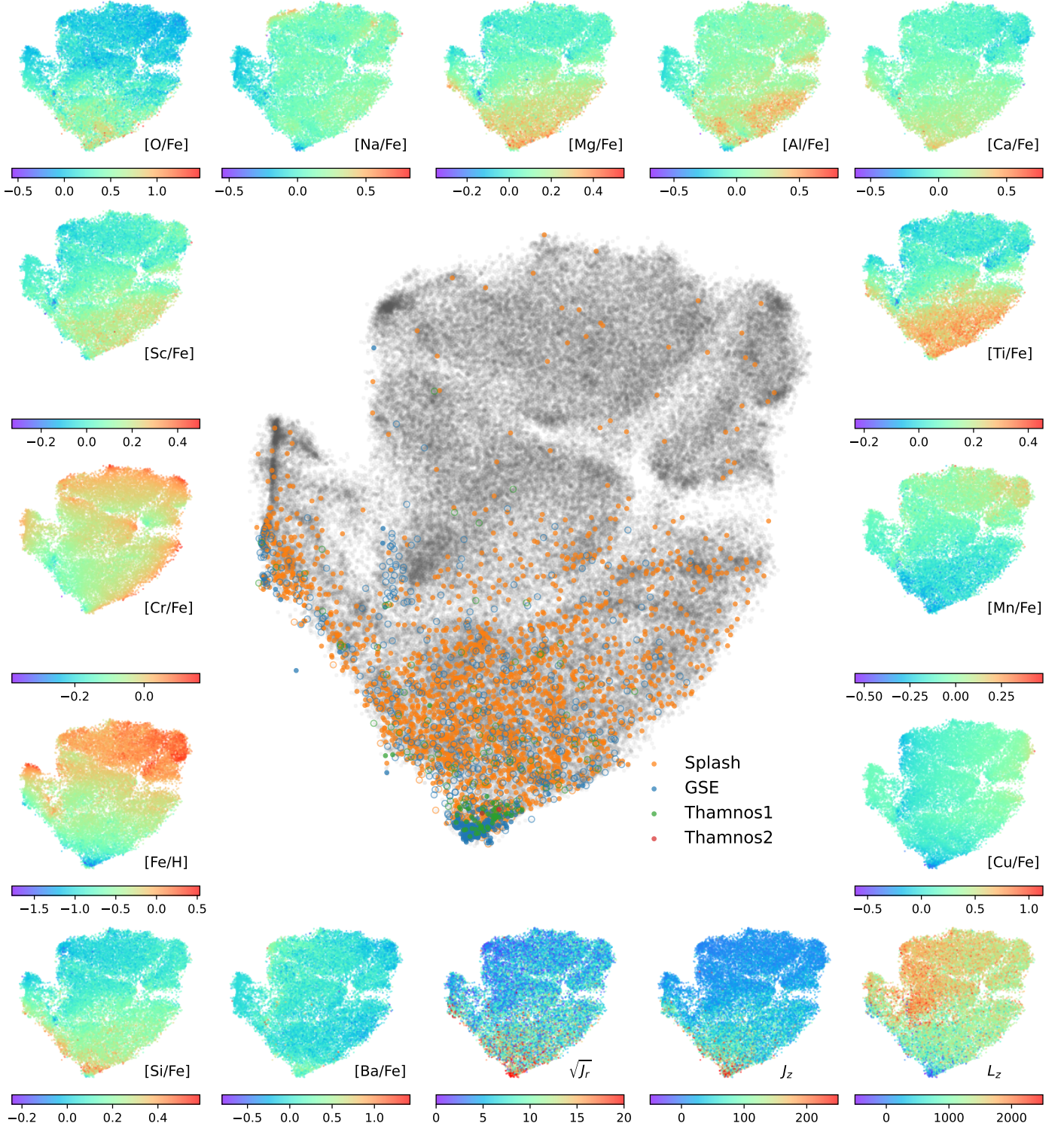


Fig. 9. t-SNE latent space projection of all stars in the GALAH sample, shown in gray. Halo stars from GSE and Thamnos1 and 2 are shown in blue, green and red, respectively, while disk stars from the Splash are shown in orange. Filled points show stars identified as belonging to the halo based on the cuts applied in Figure 4, while open circles are stars selected based on their dynamics but did not pass this chemical selection. The surrounding plots show the same latent space projection, colored by various parameters.

- fall into the inner Galaxy, and the GSE population covers the broadest range of Galactic radii and extends at least up to 15 kpc from the Galactic center.
- Stars in the Splash exhibit chemical properties of the Galactic disk, among which is high metallicity above -0.5 dex and a relatively high abundance of iron-peak elements.

- Chemical peculiarities of GSE include low-metallicity, high $[\text{Li}/\text{Fe}]$ abundance and high abundance of an r-process element Sm. Surprisingly, we observe a relatively high abundance of some s-process elements, such as Ce in GSE, which does not agree with previous studies like [Matsuno et al. \(2021\)](#).

- Thamnos has a slightly elevated $[\alpha/\text{Fe}]$ ratio than the rest of the accreted groups. Among other chemical peculiarities of the Thamnos population are abundances of Li, Ru, and Zr, which are slightly elevated than those of the rest of the groups.

In recent years, significant effort has been made to identify and study the chemo-dynamical properties of the inner halo structures. The GALAH and *Gaia* surveys play a crucial role in searching for and analyzing kinematic parameters and elemental abundances of stars within accreted stellar populations. With these surveys, the remnants of accreted populations can be easily found in the Solar vicinity. Great hope relies on future spectroscopic programs to cover a broader range of Galactocentric distances, reaching as far as $R > 20$ kpc to study the outer parts of the stellar halo. The high-precision spectroscopic data of future missions like 4MOST de Jong et al. (2019) and WEAVE Dalton et al. (2018, 2020) will hopefully shed more light on the nature of these unique building blocks of our Galaxy.

Data availability

The GALAH DR4 catalog is available at <https://www.galah-survey.org/dr4/overview/> and at the Strasbourg Astronomical Data Center (CDS) via <https://cds.unistra.fr>. We provide a supplementary table containing information for 116 047 stars with GALAH DR4 and Gaia DR3 identifiers. The column “halo” indicates whether a star belongs to the stellar halo (True) or the disk (False) based on $[\text{Mg}/\text{Cu}]$ vs. $[\text{Na}/\text{Fe}]$ criteria. The columns “Splash”, “GSE”, “Thamnos1”, and “Thamnos2” indicate whether a star belongs to the corresponding kinematic structure (True or False) based on the wavelet transform. The table is only available in electronic form and can be retrieved from the CDS via anonymous ftp to cdsarc.u-strasbg.fr (130.79.128.5) or via <http://cdsweb.u-strasbg.fr/cgi-bin/qcat?J/A+A/>.

Acknowledgements. We acknowledge the traditional owners of the land on which the AAT stands, the Gamilaraay people, and pay our respects to elders past and present. This work was partly supported by the Australian Research Council Centre of Excellence for All Sky Astrophysics in 3 Dimensions (ASTRO 3D) through project number CE170100013. IK, KY, and KL acknowledge funding from the European Research Council (ERC) under the European Union’s Horizon 2020 research and innovation program (Grant Agreement No. 852977). SB acknowledges support from the Australian Research Council under grant number DE240100150. JBH is funded by an ARC Laureate Fellowship. ZT acknowledges support from the Slovenian Research Agency (core funding No. P1-0188). DZ is funded by ARC Discovery Project DP220102254. SLM acknowledges the support of the Australian Research Council through Discovery Project grant DP220102254 and the UNSW Scientia Fellowship Program.

References

Abdurro’uf, Accetta, K., Aerts, C., et al. 2022, *ApJS*, 259, 35
 Antoja, T., Helmi, A., Bienayme, O., et al. 2012, *MNRAS*, 426, L1
 Bailer-Jones, C. A. L. 2023, *AJ*, 166, 269
 Bellazzini, M., Massari, D., De Angeli, F., et al. 2023, *A&A*, 674, A194
 Belokurov, V., Erkal, D., Evans, N. W., Koposov, S. E., & Deason, A. J. 2018, *MNRAS*, 478, 611
 Belokurov, V., Sanders, J. L., Fattahi, A., et al. 2020, *MNRAS*, 494, 3880
 Bennett, M. & Bovy, J. 2019, *MNRAS*, 482, 1417
 Bland-Hawthorn, J. & Tepper-García, T. 2021, *MNRAS*, 504, 3168
 Bovy, J. 2015, *ApJS*, 216, 29
 Buder, S., Kos, J., Wang, X. E., et al. 2025, *PASA*, 42, e051
 Buder, S., Lind, K., Ness, M. K., et al. 2022, *MNRAS*, 510, 2407
 Buder, S., Sharma, S., Kos, J., et al. 2021, *MNRAS*, 506, 150
 Conroy, C., Bonaca, A., Cargile, P., et al. 2019, *ApJ*, 883, 107
 Contursi, G., de Laverny, P., Recio-Blanco, A., et al. 2023, *A&A*, 670, A106

Dalton, G., Trager, S., Abrams, D. C., et al. 2020, in Society of Photo-Optical Instrumentation Engineers (SPIE) Conference Series, Vol. 11447, Ground-based and Airborne Instrumentation for Astronomy VIII, ed. C. J. Evans, J. J. Bryant, & K. Motohara, 1144714
 Dalton, G., Trager, S., Abrams, D. C., et al. 2018, in Society of Photo-Optical Instrumentation Engineers (SPIE) Conference Series, Vol. 10702, Ground-based and Airborne Instrumentation for Astronomy VII, ed. C. J. Evans, L. Simard, & H. Takami, 107021B
 de Jong, R. S., Agertz, O., Berbel, A. A., et al. 2019, *The Messenger*, 175, 3
 De Silva, G. M., Freeman, K. C., Bland-Hawthorn, J., et al. 2015, *MNRAS*, 449, 2604
 Deason, A. J. & Belokurov, V. 2024, *New A Rev.*, 99, 101706
 Feltzing, S. & Feuillet, D. 2023, *ApJ*, 953, 143
 Feuillet, D. K., Feltzing, S., Sahlholdt, C. L., & Casagrande, L. 2020, *MNRAS*, 497, 109
 Feuillet, D. K., Sahlholdt, C. L., Feltzing, S., & Casagrande, L. 2021, *MNRAS*, 508, 1489
 Freeman, K. & Bland-Hawthorn, J. 2002, *ARA&A*, 40, 487
 Gaia Collaboration, Vallenari, A., Brown, A. G. A., et al. 2023, *A&A*, 674, A1
 Haywood, M., Di Matteo, P., Lehnert, M. D., et al. 2018, *ApJ*, 863, 113
 Helmi, A. 2020, arXiv e-prints, arXiv:2002.04340
 Helmi, A., Babusiaux, C., Koppelman, H. H., et al. 2018, *Nature*, 563, 85
 Helmi, A., White, S. D. M., de Zeeuw, P. T., & Zhao, H. 1999, *Nature*, 402, 53
 Hinton, G. & Roweis, S. 2002, *Advances in Neural Processing Systems*, 15, 833
 Holtzman, J. A., Hesselquist, S., Shetrone, M., et al. 2018, *AJ*, 156, 125
 Horta, D., Schiavon, R. P., Mackereth, J. T., et al. 2021, *MNRAS*, 500, 1385
 Horta, D., Schiavon, R. P., Mackereth, J. T., et al. 2023, *MNRAS*, 520, 5671
 Ji, A. P., Li, T. S., Hansen, T. T., et al. 2020, *AJ*, 160, 181
 Kobayashi, C., Karakas, A. I., & Lugaro, M. 2020, *ApJ*, 900, 179
 Koppelman, H., Helmi, A., & Veljanoski, J. 2018, *ApJ*, 860, L11
 Koppelman, H. H., Helmi, A., Massari, D., Price-Whelan, A. M., & Starkenburg, T. K. 2019, *A&A*, 631, L9
 Kos, J., Bland-Hawthorn, J., Freeman, K., et al. 2018, *MNRAS*, 473, 4612
 Kushniruk, I. & Bensby, T. 2019, *A&A*, 631, A47
 Kushniruk, I., Schirmer, T., & Bensby, T. 2017, *A&A*, 608, A73
 Lane, J. M. M., Bovy, J., & Mackereth, J. T. 2023, *MNRAS*, 526, 1209
 Lee, G., Gommers, R., Waselewski, F., Wohlfahrt, K., & O’Leary, A. 2019, *The Journal of Open Source Software*, 4, 1237
 Lindegren, L., Lammers, U., Bastian, U., et al. 2016, *A&A*, 595, A4
 Matsuno, T., Hirai, Y., Tarumi, Y., et al. 2021, *A&A*, 650, A110
 Molaro, P., Cescutti, G., & Fu, X. 2020, *MNRAS*, 496, 2902
 Myeong, G. C., Vasiliev, E., Iorio, G., Evans, N. W., & Belokurov, V. 2019, *MNRAS*, 488, 1235
 Naidu, R. P., Conroy, C., Bonaca, A., et al. 2020, *ApJ*, 901, 48
 Nissen, P. E., Amarsi, A. M., Skúladóttir, Á., & Schuster, W. J. 2024, *A&A*, 682, A116
 Nissen, P. E. & Schuster, W. J. 2010, *A&A*, 511, L10
 Ortigoza-Urdaneta, M., Vieira, K., Fernández-Trincado, J. G., et al. 2023, *A&A*, 676, A140
 Pedregosa, F., Varoquaux, G., Gramfort, A., et al. 2011, *Journal of Machine Learning Research*, 12, 2825
 Ramos, P., Antoja, T., & Figueras, F. 2018, *A&A*, 619, A72
 Sanders, J. L., Belokurov, V., & Man, K. T. F. 2021, *MNRAS*, 506, 4321
 Simpson, J. D., Martell, S. L., Buder, S., et al. 2021, *MNRAS*, 507, 43
 Starck, J.-L. & Murtagh, F. 2006, *Astronomical Image and Data Analysis*
 Tolstoy, E., Hill, V., & Tosi, M. 2009, *ARA&A*, 47, 371
 Trick, W. H., Coronado, J., & Rix, H.-W. 2019, *MNRAS*, 484, 3291
 van der Maaten, L. & Hinton, G. 2008, *Journal of Machine Learning Research*, 1, 1
 van der Walt, S., Schönberger, J. L., Nunez-Iglesias, J., et al. 2014, *PeerJ*, 2, e453
 Youakim, K., Lind, K., & Kushniruk, I. 2023, *MNRAS*, 524, 2630
 Zhao, G., Zhao, Y.-H., Chu, Y.-Q., Jing, Y.-P., & Deng, L.-C. 2012, *Research in Astronomy and Astrophysics*, 12, 723